We are IntechOpen, the world's leading publisher of Open Access books Built by scientists, for scientists

4,800
Open access books available

122,000
International authors and editors

135M
Downloads

Our authors are among the

154
Countries delivered to

TOP 1%
most cited scientists

12.2%
Contributors from top 500 universities

CLARIVATE ANALYTICS BOOK CITATION INDEX INDEXED

WEB OF SCIENCE™

Selection of our books indexed in the Book Citation Index in Web of Science™ Core Collection (BKCI)

Interested in publishing with us?
Contact book.department@intechopen.com

Numbers displayed above are based on latest data collected.
For more information visit www.intechopen.com

21

Kalman Filtering for Manufacturing Processes

Thomas Oakes, Lie Tang, Robert G. Landers and S. N. Balakrishnan
Missouri University of Science and Technology
United States of America

1. Introduction

Unwanted signal variation commonly occurs in manufacturing process measurements. This variation, due to both random electrical noise and noise in the manufacturing process itself, can be quantified by calculating the steady–state process data variance

$$\sigma^2 = \frac{1}{N-1}\sum_{k=1}^{N}\left(x_k - \bar{x}\right)^2 \tag{1}$$

where x_k is the measurement at iteration k, $\bar{x}$ is the measurement average, and N is the number of samples. Noise due to the manufacturing process itself is often greater in magnitude than the electrical noise. Examples of process noise include: (1) high frequency cyclic variations due to tool eccentricity in a turning process, (2) low frequency variations due to discrete solidification of deposited material in Laser Metal Deposition (LMD) processes, and (3) chaotic mixing of materials in Friction Stir Welding (FSW) processes.

Manufacturing process measurements must be filtered before the data can be used for dynamic modeling or control. First principle modeling is generally unable to capture inherent nonlinear dynamics such as non–uniform friction and system wear. Therefore, dynamic manufacturing process models are often developed empirically. Estimation techniques such as Recursive Least Squares and Particle Swarm Optimization are commonly used for system identification to create a "best fit" model based on collected measurements. However, the fidelity of an empirical model greatly depends upon the measurements used to create it and processes with high–magnitude variations in the measurement signals are often difficult to model due to the low signal–to–noise ratio. Manufacturing process models are often used to design process controllers. Process control is the on–line adjustment of process parameters to enhance operation productivity and improve part quality. Variations in the measurement signal are generally higher in frequency than the available actuator bandwidth, which can lead to increased actuator wear and possible instability. A filter must be developed for (1) post processing of data to compensate for large signal variations prior to use by a model identification method and (2) on–line filtering capable of preserving signal phase and magnitude with minimal computational burden.

The fourth–order Butterworth filter is used in a number of manufacturing processes. Bhattacharyya and Sengupta (2007) used a fourth–order Butterworth filter on a face milling process to remove high frequency variation due to spindle rotation harmonics. Liang et al. (2002) employed a Butterworth filter on the spindle power signal of an end milling process for use in a fuzzy logic controller. Ghosh et al. (2007) used a Butterworth filter for neural–

Source: Kalman Filter: Recent Advances and Applications, Book edited by: Victor M. Moreno and Alberto Pigazo,
ISBN 978-953-307-000-1, pp. 584, April 2009, I-Tech, Vienna, Austria

based sensor fusion to estimate tool wear. Another common filter is a point–averaging filter. Freitag (2004) used a 50 ms Finite Impulse Response moving average filter to smooth command signals sent to the process controller of a miniature ball end mill. Zhao et al. (2007) employed a five–point moving average filter to reduce the standard deviation of the axial force signal of a FSW process for the purposes of modeling and process control.
The objective of this chapter is to present a methodology for filtering manufacturing process measurement signals. The rest of the chapter is organized as follows. A general filtering methodology is established that uses a stochastic model and a two–step Kalman filter. The filtering methodology is compared to other common filters via simulation studies. Post process filtering is performed on FSW and LMD processes to develop dynamic process models. Then, on–line filtering is performed for FSW and LMD processes for use in process controllers.

2. Filtering methodology

Unlike standard frequency–based filters, the Kalman filter is a time domain filter that recursively estimates process states using data from both a dynamic system model and collected measurements. Selection of a reliable dynamic process model is vital in maximizing the filter performance. A Markov process is a model that expresses the stochastic evolution of a system. This implies that knowledge of the present system states completely describes all relevant information necessary for the process evolution. Past and future states of a Markov Process are statistically independent. The excessive signal variation observed in many manufacturing processes leads to the realization that these processes can be modeled as Markov processes. A general stochastic model of a manufacturing process is

$$\dot{x}(t) = \lambda x(t) + w(t) \tag{2}$$

where $x(t)$ is the system state, λ is the system pole, and $w(t)$ is the process noise, which accounts for the system's stochastic nature, as well as changes in the input. It is assumed the process noise is Gaussian with a zero mean normal distribution and variance, Q. Transforming equation (2) into the discrete–time domain using a zero order hold

$$x(k) = e^{\lambda T_s} x(k-1) + w(k-1) \tag{3}$$

where k is the time step and T_s is the sample period (s). The two–step discrete–time Kalman filter uses the model

$$x(k) = Fx(k-1) + Gu(k-1) + w(k-1) \tag{4}$$

where $F = e^{\lambda T_s}$ and $u(k–1) = 0$ to fit the form of equation (3). The input term in equation (4) is set to zero to allow the process noise term to account for all deviations in the state due to model uncertainty and input changes. Equation (4) has process noise characteristics

$$w \sim N(0, Q) \qquad E\left(w(k)w(k)^T\right) = Q \tag{5}$$

The measurement is

$$y(k) = Hx(k) + v(k) \tag{6}$$

Equation (6) has measurement noise characteristics

$$v \sim N(0, R) \qquad E\left(v(k)v(k)^T\right) = R \tag{7}$$

where R is the measurement variance. Initial values of the state estimate and covariance, respectively, are

$$\hat{x}^+(0) = x(0) \tag{8}$$

$$P^+(0) = E\left|\left(x(0) - \hat{x}^+(0)\right)\left(x(0) - \hat{x}^+(0)\right)^T\right| \tag{9}$$

where $\hat{x}^+$ is the state estimate after the filter's measurement update (aposteriori) and P^+ is the covariance after the filter's measurement update. A large initial covariance matrix is required to ensure the estimates convergence. Equation (4) is rewritten in terms of its estimates

$$\hat{x}^-(k) = e^{\lambda T}\hat{x}^+(k-1) \tag{10}$$

where $\hat{x}^-$ is the state estimate before the filter's measurement update (apriori). Equation (10) is used to propagate the state estimate to the next time step. The covariance is propagated to the next time step using

$$P^-(k) = FP^+(k-1)F^T + Q \tag{11}$$

where P^- is the covariance prior to the filter's measurement update. The Kalman gain matrix is

$$K(k) = P^-(k)H^T\left[HP^-(k)H^T + R\right] \tag{12}$$

Then the measurement is used to update, respectively, the state estimate and covariance

$$\hat{x}^+(k) = \hat{x}^-(k) + K(k)\left[y(k) - H\hat{x}^-(k)\right] \tag{13}$$

$$P^+(k) = \left[I - K(k)H\right]P^-(k)\left[I - K(k)H\right]^T + K(k)RK^T(k) \tag{14}$$

The computations in equations (10)–(14) are repeated at each time step.

2.1 Filter tuning

A generic first order system is used to illustrate the tuning required for the filtering methodology. The system's transfer function is

$$G(s) = \frac{K}{\tau s + 1} = \frac{6}{0.6s + 1} \tag{15}$$

where K is the gain and τ is the time constant. The system is converted into the discrete–time domain using a zero order hold and T_s = 0.01 s

$$G(z) = \frac{9.917 \cdot 10^{-2}}{z - 0.9835} \tag{16}$$

The unit step response is shown in Fig. 1. Random noise with variance 0.25 is added to the output to simulate a noisy measurement. The measurement variance, R, is calculated directly from the measurement data while values of λ and Q are tuned to optimize the filter's performance. This can be accomplished by first setting $Q = R$, implying equal faith in the measurements and model, and tuning λ while leaving Q and R constant until the disparity between the filtered and measured data is minimized.

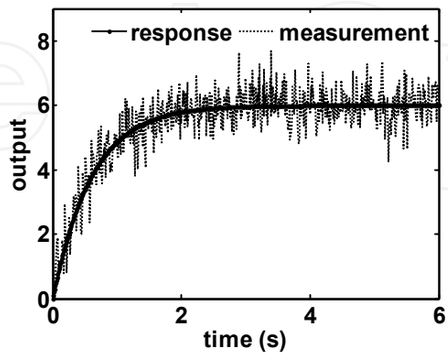

Fig. 1. Unit step response of system described by equation (16)

Figure 2 illustrates the effect of tuning λ. As λ approaches zero, the observable offset between the measurement data and the estimated state is eliminated. For this particular portion of the tuning process, it can be assumed that the optimal value of λ is zero.

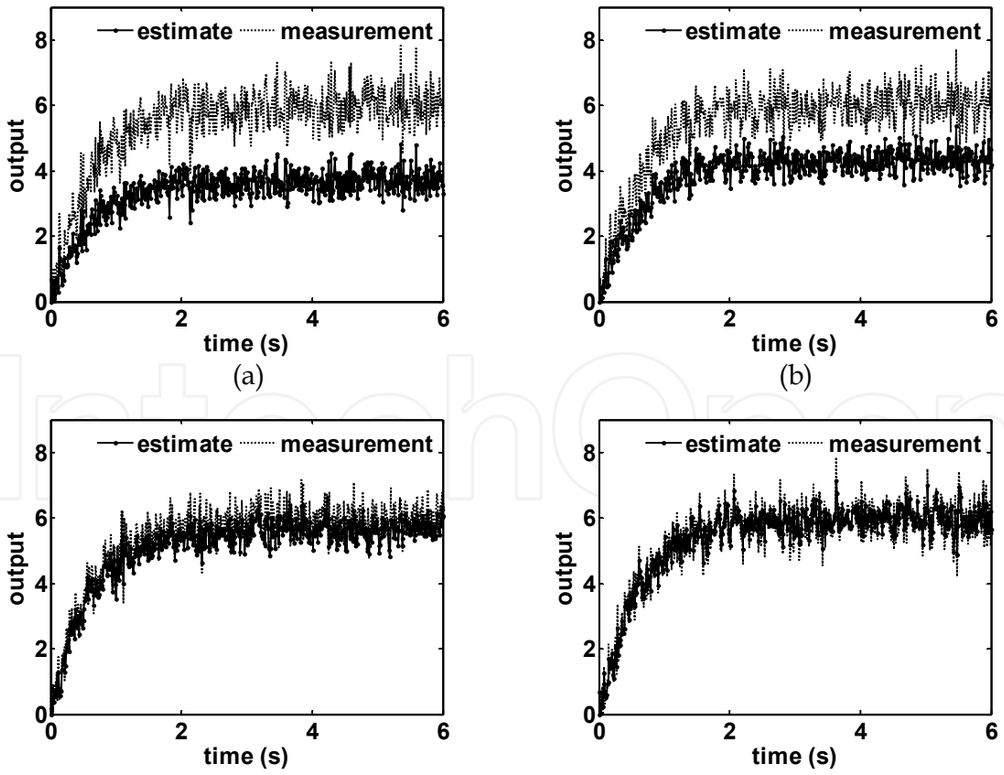

Fig. 2. Outputs and estimates for system described by equation (16) with a unit step input and (a) λ = –1000, (b) λ = –100, (c) λ = –10, and (d) λ = 0, with $Q = R = 0.25$ and $T_s = 0.01$ s

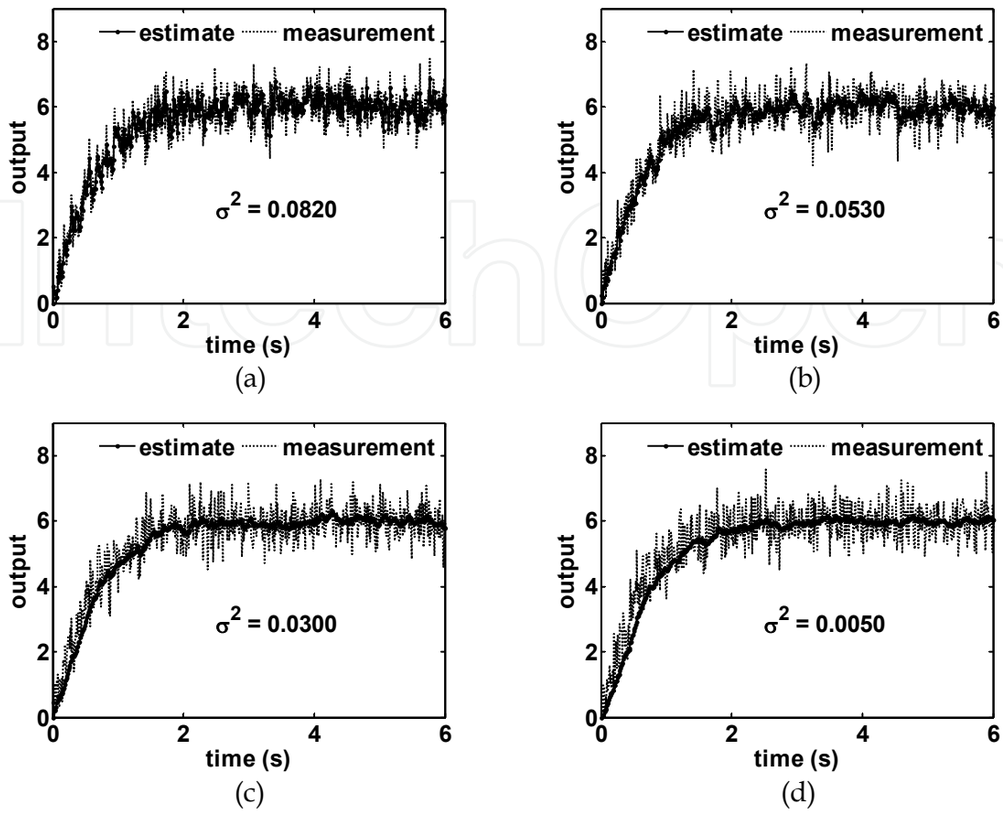

Fig. 3. Outputs and estimates for system described by equation (16) with a unit step input and (a) $Q = 0.5R$, (b) $Q = 0.1R$, (c) $Q = 0.01R$, and (d) $Q = 0.005R$, with $\lambda = 0$ and $T_s = 0.01$ s

The sampling period also has a tremendous affect on the filter performance. Applying a zero order hold to equation (15) with $T_s = 0.1$ s

$$G(z) = \frac{0.9288}{z - 0.8465} \tag{17}$$

With $\lambda = 0$, the same tuning process of Q is performed to illustrate the affect the sample rate has on the filter performance. The results are shown in Fig. 4. The larger sample period impacts the degree to which adjusting the value of Q will affect the phase. Lowering the value of Q significantly reduces the variance when compared to Fig. 3; however, it also significantly increases the phase due to less data being available to the filter during the transient portion of the process.

2.2 Filter comparison

The performances of two common filters are compared to that of the proposed filtering methodology. A first order low–pass filter is

$$\frac{X_f(s)}{X(s)} = \frac{1}{\tau s + 1} \tag{18}$$

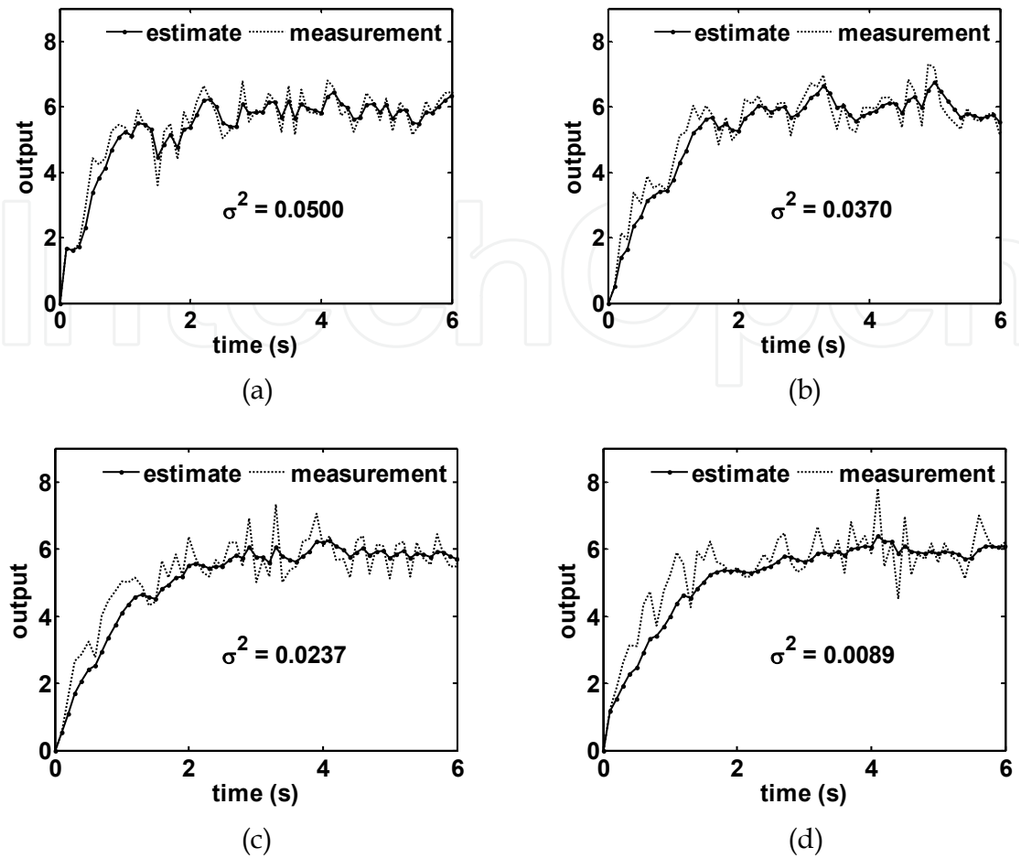

Fig. 4. Outputs and estimates for system described by equation (17) with a unit step input and (a) $Q = 0.5R$, (b) $Q = 0.25R$, (c) $Q = 0.1R$, and (d) $Q = 0.05R$, with $\lambda = 0$ and $T_s = 0.1$ s

where $X_f(s)$ is the filtered signal, $X(s)$ is the unfiltered signal, τ is the time constant and τ–1 is the filter break frequency (rad/s). The break frequency is selected to be 2π to provide a cut off frequency of 1 Hz; therefore, $\tau = 0.1592$ s. Transforming equation (18) into the discrete–time domain with a zero order hold and $T_s = 0.01$ s

$$\frac{X_f(z)}{X(z)} = \frac{6.882 \cdot 10^{-2}}{z - 0.9391} \tag{19}$$

Transforming equation (18) into the discrete–time domain with a zero order hold and T_s = 0.01 s

$$\frac{X_f(z)}{X(z)} = \frac{0.4664}{z - 0.5336} \tag{20}$$

A fourth–order Butterworth filter with a 1 Hz cutoff frequency and $T_s = 0.01$ s is

$$\frac{X_f(z)}{X(z)} = \frac{8.982 \cdot 10^{-7} z^4 + 3.594 \cdot 10^{-6} z^3 + 5.391 \cdot 10^{-6} z^2 + 3.594 \cdot 10^{-6} z + 8.982 \cdot 10^{-7}}{z^4 - 3.836 z^3 + 5.521 z^2 - 3.534 z + 0.8486} \tag{21}$$

A fourth order Butterworth filter with a 1 Hz cutoff frequency and $T_s = 0.1$ s is

$$\frac{X_f(z)}{X(z)} = \frac{4.824\cdot10^{-3}z^4 + 1.937\cdot10^{-2}z^3 + 2.891\cdot10^{-2}z^2 + 1.937\cdot10^{-2}z + 4.824\cdot10^{-3}}{z^4 - 2.366z^3 + 2.314z^2 - 1.055z + 0.1874} \quad (22)$$

Plots of filters' performances are shown for the transient portion of the response in Fig. 5 for T_s = 0.01 s and in Fig 6 for T_s = 0.1 s. Values of Q = 0.01 and Q = 0.25 are selected for the Kalman filter with T_s = 0.01 and 0.1 s, respectively. Figures 5 and 6 show that the filtering methodology outperforms the low–pass and Butterworth filters. All three filters underpredict the measurement for both sample periods. The maximum error of the Butterworth filter is approximately 44% for both sample periods while the low–pass and Kalman filters contain comparable maximum errors at approximately 13%. Less error is present in the Kalman filter estimates in both plots through the majority of the transient portion of the response.

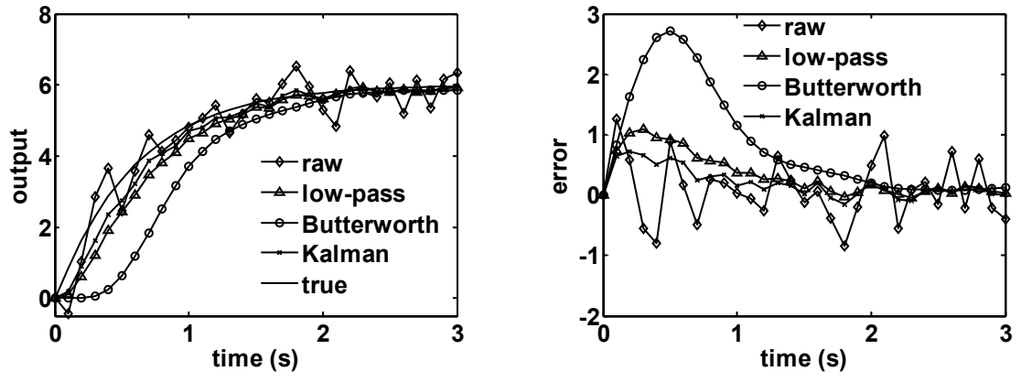

(a) (b)

Fig. 5. (a) Output and (b) error for low–pass, Butterworth, and Kalman filters, T_s = 0.01 s

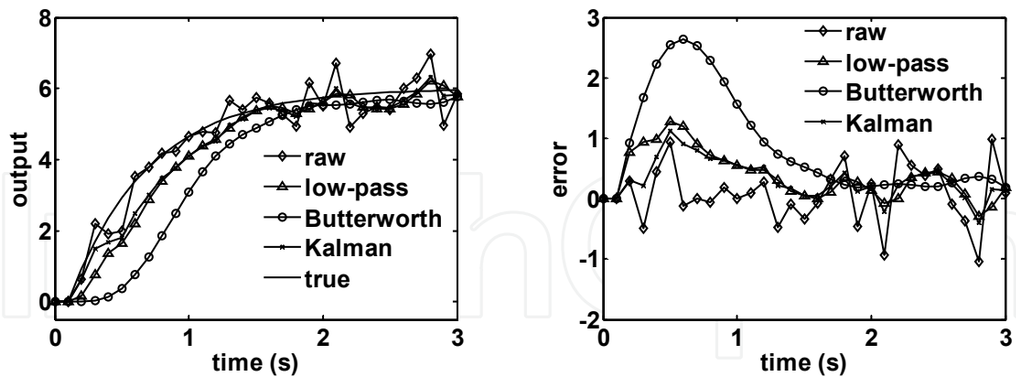

(a) (b)

Fig. 6. (a) Output and (b) error for low–pass, Butterworth, and Kalman filters, T_s = 0.1 s

2.3 Modeling

The Recursive Least Squares technique (Åström & Wittenmark, 1995) is used to develop system models from the filtered and raw signals. The model responses for a step input are shown in Figs. 7 and 8 for T_s = 0.01 and 0.1 s, respectively. The model coefficients and percent error are shown in Tables 1 and 2 for T_s = 0.01 and 0.1 s, respectively. The model

constructed from the data processed with the Kalman filter is the most accurate in terms of coefficient estimates, transient response, and steady–state error. The model constructed from the data processed with the Butterworth filter has significant errors due to the phase shift created by the Butterworth filter. The model constructed from the raw data contains the most error since the noise distorts the system dynamics.

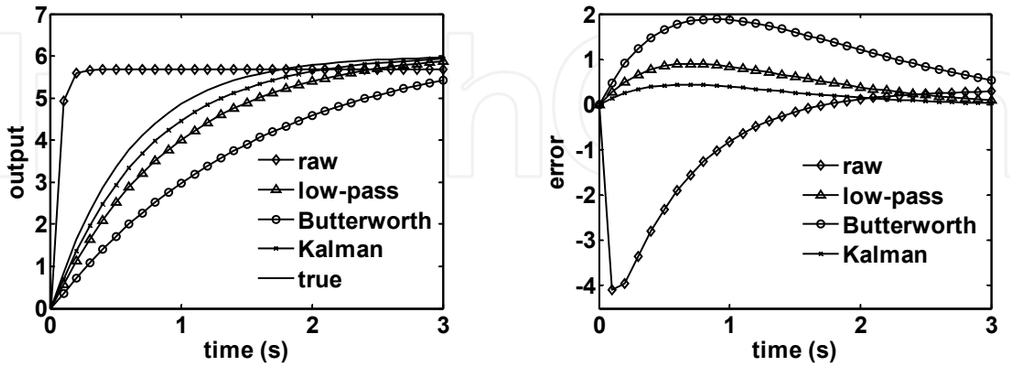

(a) (b)

Fig. 7. Model (a) output and (b) error using raw data, low–pass, Butterworth, and Kalman filters, T_s = 0.01 s

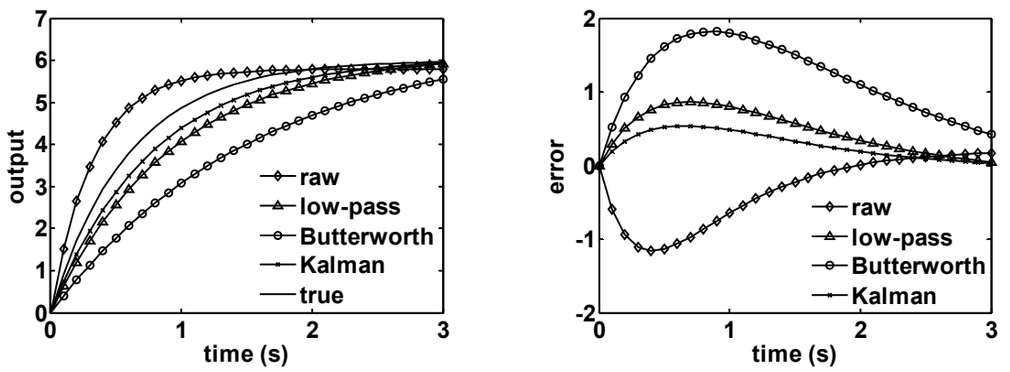

(a) (b)

Fig. 8. Model (a) output and (b) error using raw data, low–pass, Butterworth, and Kalman filters, T_s = 0.1 s

	a		b	
	estimate	error (%)	estimate	error (%)
raw data	-0.797	19.0	1.15	1060
low-pass	-0.989	0.596	$6.57 \cdot 10^{-2}$	34.1
Butterworth	-0.994	1.04	$4.05 \cdot 10^{-2}$	59.3
Kalman	-0.986	0.315	$8.15 \cdot 10^{-2}$	18.2

Table 1. Coefficient estimates for models with T_s = 0.01 s, a = –0.983, and b = 9.917 ·10–2

	a		b	
	estimate	error (%)	estimate	error (%)
raw data	-0.737	12.9	1.52	64.8
low-pass	-0.897	6.04	0.631	31.5
Butterworth	-0.938	10.8	0.404	56.2
Kalman	-0.879	3.88	0.732	20.6

Table 2. Coefficient estimates for models with T_s = 0.01 s, a = –0.846, and b = 0.922

The filtering methodology can be used to filter data prior to empirical modeling to acquire a more reliable model. Since this filter relies on model–based estimation, it has always been necessary to have a precise model of the system dynamics to ensure proper filter performance. However, the stochastic process model provides a way to use a Kalman filter for state estimation with limited knowledge of the system behavior.

3. Friction Stir Welding example

Friction Stir Welding is a new welding technique capable of joining traditionally hard to join materials such as 2000 and 7000 series aluminum alloys (Mishra & Ma, 2005). The process utilizes a rotating, non–consumable tool containing a shoulder and profiled pin to induce gross plastic deformation along a weld path. In a FSW process, the tool is plunged into the material at a specified spindle speed, ω, until the shoulder contacts the material and is then left to dwell for a specified period of time to soften the surrounding area. The tool then advances along its weld path at a traverse speed, v, joining the material as it leaves the processing zone. Schematics of the FSW process are shown in Fig. 9.

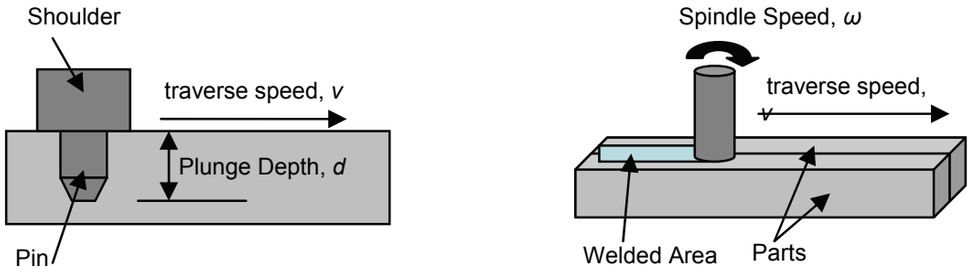

Fig. 9. FSW Process Schematics

Constant process parameter runs in FSW processes can lead to internal defects known as wormholes and surface voids due to improper fixturing of the parts and machine geometric errors. Therefore, the process is typically run in a force control mode in which the traverse speed and spindle speed are held constant while the plunge depth is adjusted on–line to maintain a desired axial force profile. Before a controller can be designed, the system is modeled empirically through a series of step tests. An example of a step test is shown in Fig. 10. It can be seen that small changes in plunge depth create large changes in axial force. If no

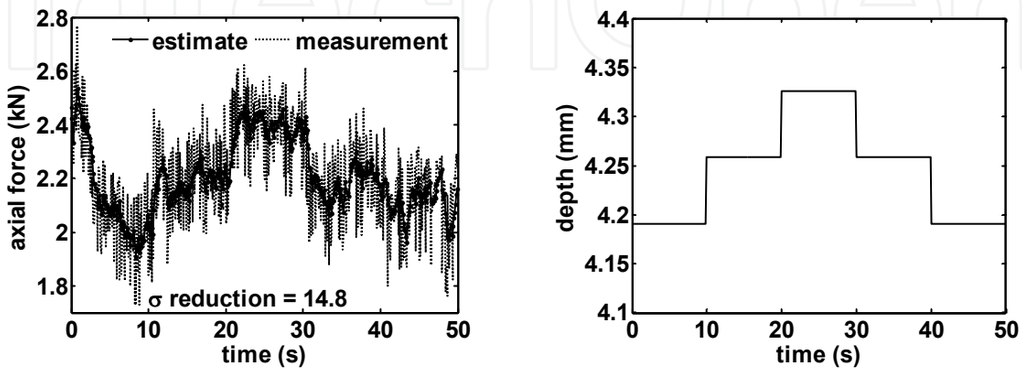

(a) (b)

Fig. 10. FSW step test (a) axial force and (b) plunge depth, v = 2.6 mm/s and ω = 1600 rpm

post signal processing is used, the combined process and sensor noise is so large in magnitude that it is difficult to detect changes in the axial force due to changes in the plunge depth. This is particularly apparent between the fourth and fifth step changes. From the experimental data, $R = 1.63 \cdot 10^{-2}$ kN^2. The filtering methodology is applied using $\lambda = 0$ and $Q = 0.05R$ to the measurement data in Fig. 10. It is seen that the variance is greatly reduced (i.e., nearly a factor of fifteen) without compromising the phase and magnitude fidelity.

3.a FSW process modeling

Twelve experiments are conducted based on a central composite Design of Experiments (DOE) over the operating range of all three process parameters. The filtering methodology is applied with $\lambda = 0$ and $Q = 0.05R$ to all twelve runs. Table 3 shows the process parameters, heat index, and variance reduction ratio for each run. The variance reduction ratio is the unfiltered signal variance divided by the filtered signal variance. The results demonstrate the filtering methodology can reduce signal variance by a factor of 3 to nearly a factor of seventeen for FSW processes.

The results from runs 11 and 12 were deemed to be unacceptable and, therefore, were not used to create the dynamic model. This can be explained by the heat index, which is

$$HI = \frac{\omega^2}{10^4 v} \tag{23}$$

Note the traverse speed is given in inches per minute when calculating the heat index. Runs 11 and 12 had particularly low heat indices, although they were not the lowest. A low heat index can lead to a "cold run" that sometimes produces poor welds.

Run	v (mm/s)	ω (rpm)	HI (rpm^2/ipm)	Variance Reduction Ratio
1	2.60	1600	41.7	11.3
2	2.60	1900	58.8	3.11
3	2.18	1810	63.6	4.91
4	3.02	1390	27.1	12.9
5	2.60	1600	41.7	7.08
6	3.02	1810	45.9	8.25
7	2.18	1390	37.5	16.9
8	3.02	1390	27.1	5.22
9	2.18	1810	63.6	3.07
10	2.00	1600	54.2	7.23
11	3.20	1600	33.9	12.1
12	2.60	1300	27.5	6.01

Table 3. Process parameters and variance reduction ratio for FSW runs used for process modeling

An empirical second order model of the process and equipment dynamics is

$$\frac{F(z)}{U(z)} = v^{\alpha}\omega^{\beta}\frac{b_1 z + b_2}{z^2 + a_1 z + a_2} z^{-n_d} \tag{24}$$

where $F(z)$ is the axial force, $U(z)$ is the control signal, n_d is the number of delay periods, and b_1, b_2, a_1, a_2, a, and β are model coefficients. The model structure is based upon visual inspection of the runs in Table 3. The control signal and plunge depth are related by

$$u(k) = d^{\gamma}(k) \tag{25}$$

where γ is a model coefficient. The model coefficients α, β, and γ are found by using the steady–state model

$$F_{ss} = Cv^{\alpha}\omega^{\beta}d^{\gamma} \tag{26}$$

where F_{ss} is the average steady–state axial force and C is the steady–state gain. Taking the natural log of both sides of equation (19)

$$\ln(F_{ss}) = \ln(C) + \alpha\ln(v) + \beta\ln(\omega) + \gamma\ln(d) \tag{27}$$

and applying Least Squares to the data in runs 1–10, $C = 6.18 \cdot 10^{-2}$, $\alpha = 0.185$, $\beta = -0.374$, and $\gamma = 2.65$. Transforming equation (24) into the discrete–time domain

$$F(k) = -a_1F(k-1) - a_2F(k-2) + v^{\alpha}\omega^{\beta}\left[b_1u(k-1-n_d) + b_2u(k-2-n_d)\right] \tag{28}$$

where n_d is determined to be 5 iterations by visually inspecting the step tests. Recursive Least Squares is used to determine the model coefficients $b1$, $b2$, $a1$, and $a2$. A complete covariance reset is employed if any of the diagonals of the covariance matrix become less than ten percent of their initial value. After the algorithm is executed for runs 1–10, the model coefficient sets are averaged and the transfer function is

$$\frac{F(z)}{U(z)} = v^{0.185}\omega^{-0.374}\frac{1.22\cdot10^{-2}z}{z^2 - 0.848z + 4.77\cdot10^{-2}}z^{-5} \tag{29}$$

The empirical model is now constructed in the same manner as above using the unfiltered data. In this case the transfer function is

$$\frac{F(z)}{U(z)} = v^{0.189}\omega^{-0.372}\frac{6.04\cdot10^{-2}z - 6.2\cdot10^{-3}}{z^2 - 7.34\cdot10^{-2}z - 3.48\cdot10^{-2}}z^{-5} \tag{30}$$

The response of each model is now compared to the measured data. An example is shown in Fig. 11. Both dynamic models predict steady–state values within five percent of each other.

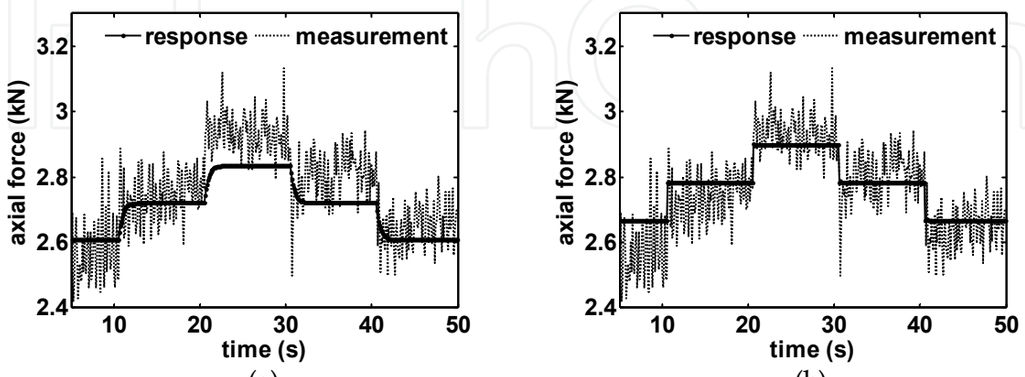

Fig. 11. Measured response compared to (a) response of model developed using filtered data and (b) response of model developed using unfiltered data, with v = 3.02 mm/s, ω = 1810 rpm, and plunge depth profile in Fig. 10b.

The model in equation (29) contains two overdamped poles with time constants of $3.57 \cdot 10^{-2}$ and 0.418 s. The model in equation (30) contains two overdamped poles with time constants of $6.74 \cdot 10^{-2}$ and $5.33 \cdot 10^{-2}$ s. Based on the work of Zhao et al. (2007), the system is dominated by a time constant of 0.519 s. This implies the model acquired through the use of the unfiltered data is not reliable and should not be used for controller design.

3.b FSW process control

A general tracking controller with constant disturbance rejection is designed to control the axial force. The block diagram is shown in Fig. 12. The transfer function is

$$G(z) = \frac{b(z)}{a(z)} \tag{31}$$

The disturbance generating polynomial is

$$v(z) = z - 1 \tag{32}$$

The controller polynomial is

$$g(z) = g_1 z^2 + g_2 z + g_3 \tag{33}$$

where $g1$, $g2$, and $g3$ are chosen to shape the closed–loop system error dynamics. The closed–loop error dynamics are third order with one overdamped pole and two underdamped poles. The time constant of the overdamped pole is $\tau 1$ = 0.03 s and the two underdamped poles are characterized by a natural frequency of 10 rad/s and a damping ratio of 0.5. Equating the actual and desired closed–loop characteristic polynomials

$$v(z)a(z) - g(z) = z^3 - 0.8216z^2 + 0.3959z - 1.311 \cdot 10^{-2} \tag{34}$$

Equating like coefficients in z in equation (34), g_1 = –1.026, g_2 = 0.4994, and g_3 = –0.3460. The control signal is

$$\begin{aligned} u(k) = {} & \frac{1}{b_1}\left[F_r(k+1) + (a_1 - 1)F_r(k) + (a_2 - a_1)F_r(k-1) - a_2 F_r(k-2)\right] \\ & - \frac{1}{b_1}\left[g_1 E_1(k) - g_2 E_1(k-1) - g_3 E_1(k-2)\right] \\ & + \frac{1}{b_1}\left[(b_2 - b_1)u(k-1) + b_2 u(k-2)\right] \end{aligned} \tag{35}$$

The controller is implemented on the FSW platform with saturation limits on the plunge depth set between 4.17 mm and 4.8 mm to ensure the shoulder does not lose contact with the material surface. The imposed rate limitation on change in plunge depth is 0.5 mm/s to prevent tool breakage.

Four control experiments are now presented. In the first experiment the axial force controller uses the unfiltered measurement to track $F_r(t)$ = 2.7 kN. The traverse speed and spindle speed are 2.18 mm/s and 1810 rpm, respectively. The results are plotted in Fig. 13. The controller maintains a constant force with an average 2.74 kN and standard deviation of

0.372 kN; however, the average absolute error during the steady–state response is 0.341 kN and large axial force oscillations occur due to the large amounts of variation present in the raw measurement signal. The plunge depth signal has large oscillations and often saturates at its lower limit.

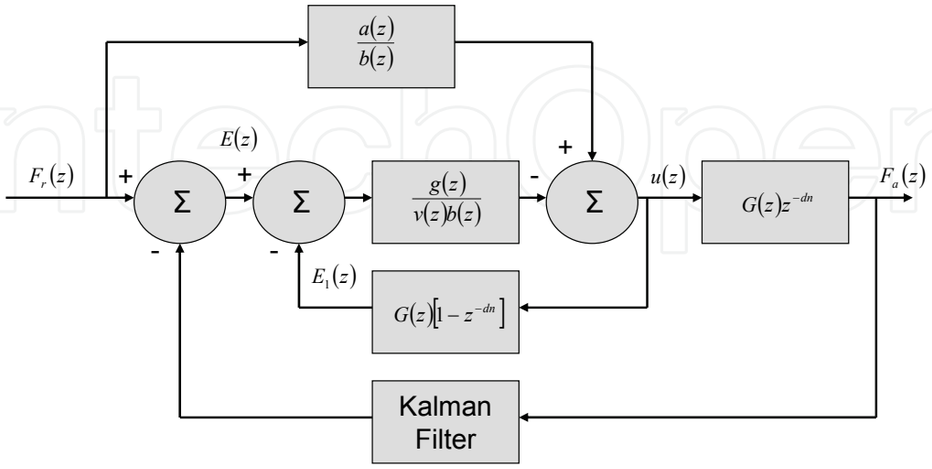

Fig. 12. Axial force closed–loop system block diagram

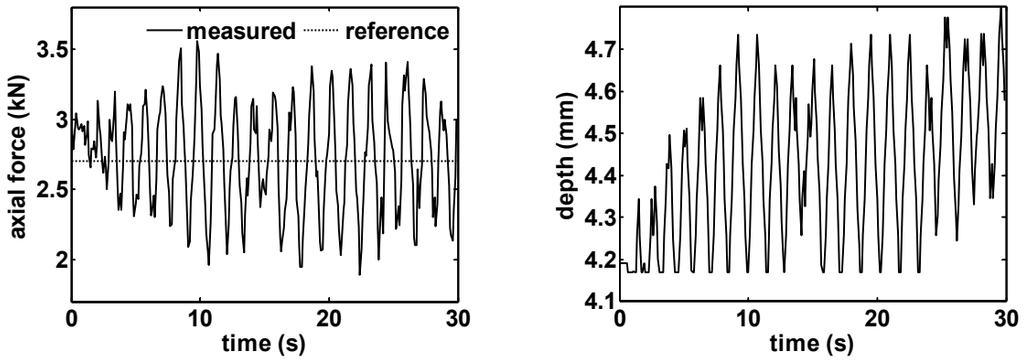

(a) (b)

Fig. 13. Axial force controller results using unfiltered measurement and $F_r(t)$ = 2.7 kN, (a) axial force and (b) plunge depth

In the second experiment the axial force controller uses the filtered measurement to track $F_r(t)$ = 2.7 kN. The traverse speed and spindle speed are 2.18 mm/s and 1810 rpm, respectively. The results are shown in Fig. 14. In this case the average axial force is 2.705 kN, the standard deviation is 0.141 kN, and the absolute average error is 0.106 kN during the steady–state response. The filter effectively reduces the magnitude of the oscillations in both the axial force and plunge depth signals. Implementation of the filtering methodology allows for a wider range of reference tracking as the controller no longer saturates.
Next, the axial force controller is used to track the time varying reference

$$F_r(t) = 2.7 + 0.1\sin(0.8\pi t) \tag{36}$$

In the third experiment the axial force controller uses the unfiltered measurement to track the reference signal in equation (36). The traverse speed and spindle speed are 2.18 mm/s

and 1810 rpm, respectively. The results are shown in Fig. 15. As in Fig. 13, the controller is able to adequately track the desired reference, but with considerable oscillations and plunge depth saturation at both its upper and lower limits. For this experiment the average absolute error is 0.413 kN during the steady–state response.

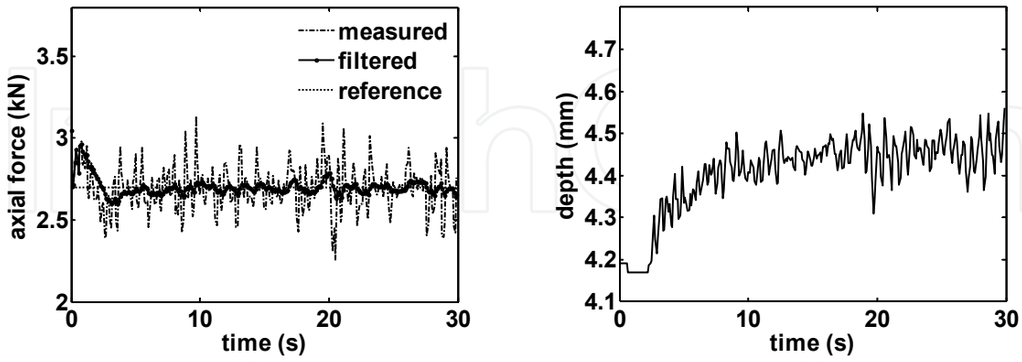

(a) (b)

Fig. 14. Axial force controller results using filtered measurement and $F_r(t)$ = 2.7 kN, (a) axial force and (b) plunge depth

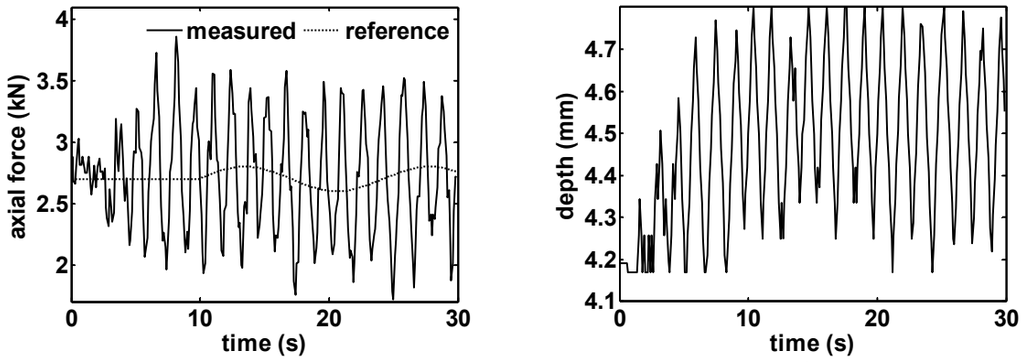

(a) (b)

Fig. 15. Axial force controller results using unfiltered measurement and reference force in equation (36), (a) axial force and (b) plunge depth

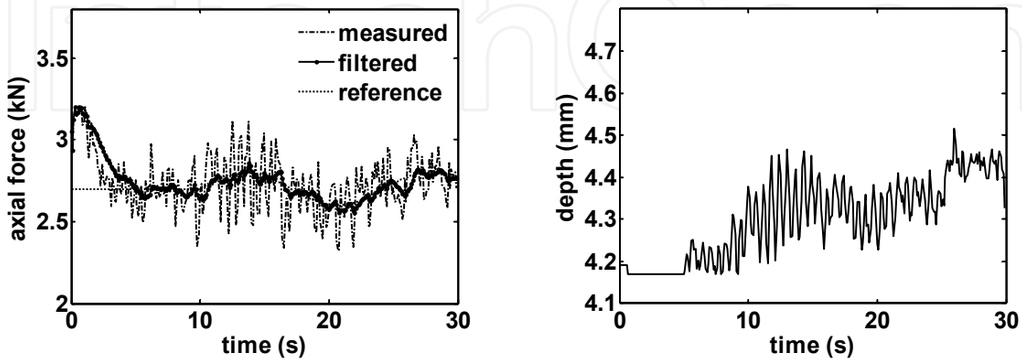

(a) (b)

Fig. 16. Axial force controller results using filtered measurement and reference force in equation (36), (a) axial force and (b) plunge depth

In the fourth experiment the axial force controller uses the filtered measurement to track the reference signal in equation (36). The traverse speed and spindle speed are 2.18 mm/s and 1810 rpm, respectively. The results are shown in Fig. 16. Similar to Fig. 14, the filter effectively reduces the magnitude of the axial force oscillations and allows for a wider range of reference signals to be utilized since the plunge depth is not saturating during the steady–state response. For this experiment the average absolute error is 0.124 kN during the steady–state response.

4. Laser metal deposition example

Laser Metal Deposition is an important Solid Freeform Fabrication technique that allows direct fabrication of functional metal parts directly from CAD solid models (Liou et al., 2007). The process can also be used for part repair, thereby extending product service life. Generally an LMD system consists of a multiple–axis motion system, a laser, and a powder feeder (see Fig. 17). During the process, a powder stream is injected into a laser generated melt pool on the substrate. With the axis moving, the melt pool quickly solidifies and forms a clad; thus, the injected powder is metallurgically bonded with the substrate. Depending on the trajectory of the motion system, parts with complex geometries can be fabricated in a layer–by–layer manner. Melt pool temperature control is an important control problem in LMD because it affects the part microstructure, which is highly related to the material properties. The measurement signal has tremendous variations that may deteriorate the controller performance. The application of the filtering methodology to the temperature measurement signal will significantly reduce measurement signal variation, resulting in improved controller performance.

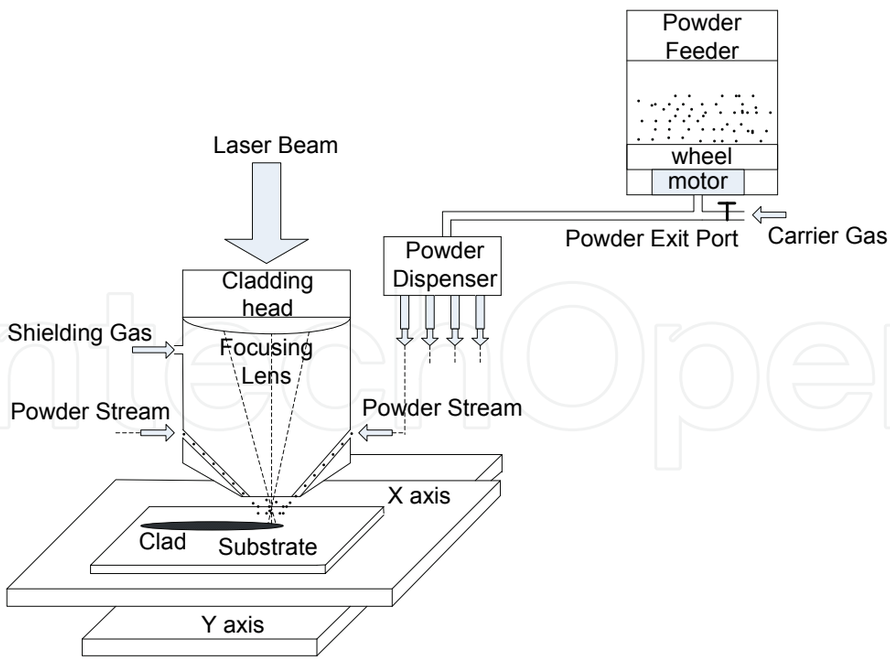

Fig. 17. LMD system schematic

To illustrate the affect the filtering methodology has on the measured temperature signal, an open–loop test is conducted. In this experiment the powder flow rate is 4 g/min and the

traverse speed is 4 ipm. The powder material is H13 tool steel with particles having a mean diameter of 100 μm. The filtered and measured temperature signals are shown in Fig. 18. The filtering methodology reduces the standard deviation from 39.2 °C in the raw signal to 30.2 °C in the filtered signal.

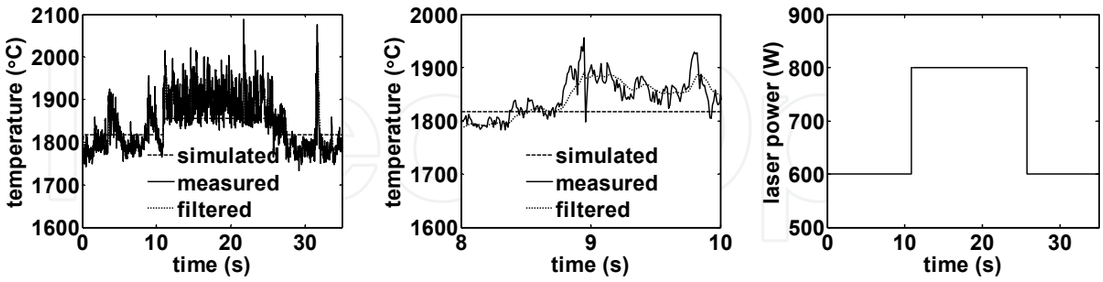

(a) (b) (c)

Fig. 18. Open–loop LMD test with T_s = 0.01 s, λ = 0, R = 2500, and Q = 25, (a) temperature versus time, (b) zoomed–in view of temperature versus time, and (c) laser power versus time

4.a LMD process modeling

The melt pool temperature is modeled using the following transfer function

$$T(s) = \frac{K}{\tau s + 1} V^{\alpha}(s) Q^{\beta}(s) M^{\gamma}(s) \tag{37}$$

where T is the melt pool temperature (°C), V is the traverse speed (ipm), Q is the laser power (W), M is the powder flow rate (g/min), K is the system gain, and τ is the time constant (s). Transforming equation (37) into the discrete–time domain using a zero order hold

$$T(z) = \frac{b_0}{z + a_0} V^{\alpha}(z) Q^{\beta}(z) M^{\gamma}(z) \tag{38}$$

where $a_0 = -e^{-T_s/\tau}$ and $b_0 = K\left(1 - e^{-T_s/\tau}\right)$. To determine the model coefficients K, a, β, and γ, the steady–state portion of equation (38) is considered

$$T_{ss} = K v^{\alpha} q^{\beta} m^{\gamma} \tag{39}$$

where T_{ss} is the average steady–state temperature. A series of experiments, covering the process operating range, are designed using DOE. The results are listed in Table 4. The parameters are estimated using the Least Squares method based on the data listed in Table 4 and are found to be K = 1170, a = –8.18·10^{-3}, β = 7.16·10^{-2}, and γ = 3.42·10^{-3}. The filtering methodology is applied to the data in Table 4 and it is seen the signal variance has been reduced by 16 to nearly 60%.

To determine the time constant, an experiment is conducted where the laser power is increased and decreased in a step–wise manner. For this experiment, m = 4 g/min and v = 4 ipm. The measured temperature data is processed using the filtering methodology with λ = 0, R = 2500, and Q = 25. Recursive Least Squares is then applied to estimate the time

constant. The value of the time constant is determined to be $\tau = 7.27 \cdot 10^{-2}$ s. The model response is compared to the filtered measurement data in Fig. 18.

Run	*Q* (W)	*m* (g/min)	*v* (ipm)	ave(*T*) (°C)	Variance Reduction (%)
1	600	4	8	1851	16.1
2	700	4	4	1861	27.4
3	800	6	4	1911	59.6
4	600	6	6	1835	22.6
5	700	8	6	1854	26.6
6	800	4	6	1854	42.6
7	600	8	4	1842	35.1
8	700	6	8	1857	33.5
9	800	8	8	1881	25.6

Table 4. Experimental results for model coefficient identification of LMD process

4.b LMD process control

Letting $U(z) = V^{\alpha}(z)Q^{\beta}(z)M^{\gamma}(z)$, equation (38) becomes

$$T(z) = \frac{b_0}{z + a_0} U(z) \tag{40}$$

A general tracking controller using the Internal Model Principle is designed to regulate the melt pool temperature. The block diagram is shown in Fig. 19.

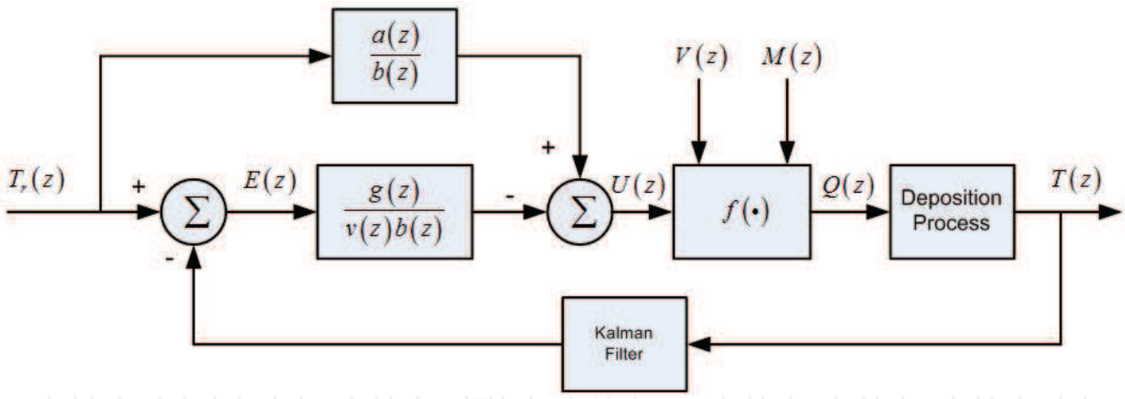

Fig. 19. Melt pool temperature closed–loop control system block diagram

With the disturbance generating polynomial given in equation (32) and a closed–loop characteristic polynomial $v(z)a(z)$–$g(z)$ with two poles located at $-e^{-T_s/\tau_1}$ and $-e^{-T_s/\tau_2}$, where $\tau_1 = 0.1$ s and $\tau_2 = 0.11$ s, the controller polynomial is

$$g(z) = g_1 z + g_0 = \left(e^{-T_s/\tau_1} + e^{-T_s/\tau_2} - 1 - e^{-T_s/\tau}\right) z + \left(e^{-T_s/\tau} - e^{-T_s/\tau_1 - T_s/\tau_2}\right) \tag{41}$$

The control signal is

$$u(k) = u(k-1) + \frac{T_r(k+1) - \left(1 + e^{-T_s/\tau}\right) T_r(k) + e^{-T_s/\tau} T_r(k-1) - g_1 e(k) - g_0 e(k-1)}{K\left(1 - e^{-T_s/\tau}\right)} \tag{42}$$

and the commanded laser power is

$$q(k) = \left(\frac{u(k)}{v(k)^{\alpha} m(k)^{r}} \right)^{1/\beta} \tag{43}$$

Four control experiments are now presented. In the first experiment the temperature controller uses the unfiltered measurement to track $T_r(t)$ = 1900 °C. The mass flow rate and traverse speed are 6 g/min and 6 ipm, respectively. The results are shown in Fig. 20. For this experiment, the average melt pool temperature is 1904 °C, the average absolute error is 61.8 °C, and error standard deviation is 76.8 °C. The results show that significant variation exists in both the temperature and the laser power signals.

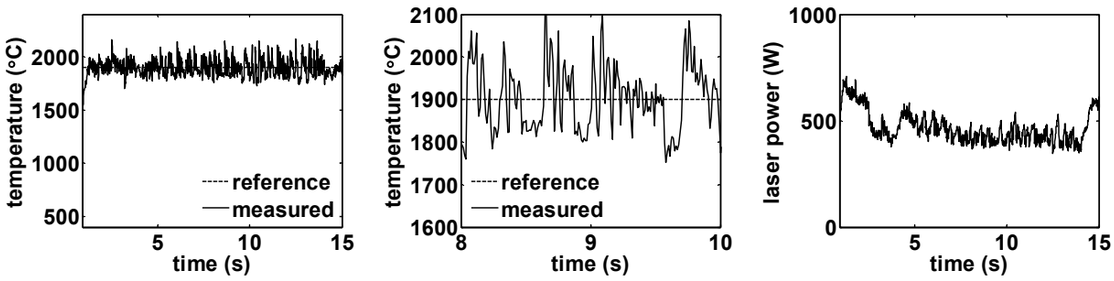

Fig. 20. Temperature controller results using unfiltered measurement and $T_r(t)$ = 1900 °C, (a) temperature, (b) zoomed–in view of temperature, and (c) laser power

In the second experiment the temperature controller uses the filtered measurement to track $T_r(t)$ = 1900 °C. The mass flow rate and traverse speed are 6 g/min and 6 ipm, respectively. The results are shown in Fig. 21. For this experiment, the average melt pool temperature is 1901 °C, the average absolute error is 42.3 °C, and error standard deviation is 57.9 °C. The results show that the average absolute error is reduced by 31.6% and the error standard deviation is reduced by 24.6%.

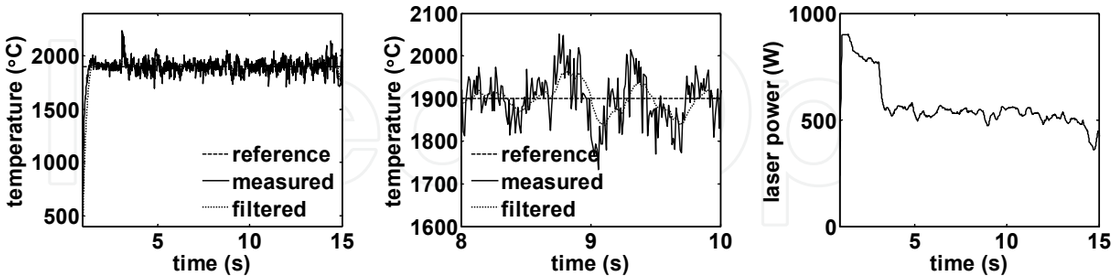

Fig. 21. Temperature controller results using filtered measurement and $T_r(t)$ = 1900 °C, (a) temperature, (b) zoomed–in view of temperature, and (c) laser power

The performances of the controllers are now compared when tracking a time varying reference. The temperature reference for these experiments is

$$T_r(t) = 1850 + 50\sin(t) \tag{44}$$

In the third experiment the temperature controller uses the unfiltered measurement to track the temperature reference given in equation (44). The mass flow rate and traverse speed are 6 g/min and 6 ipm, respectively. The results are shown in Fig. 22. The average absolute error is 52.9 °C and error standard deviation is 71.0 °C. The results show that significant variation exists in both the temperature and the laser power signals due to the fact that the controller operates on the unfiltered signal.

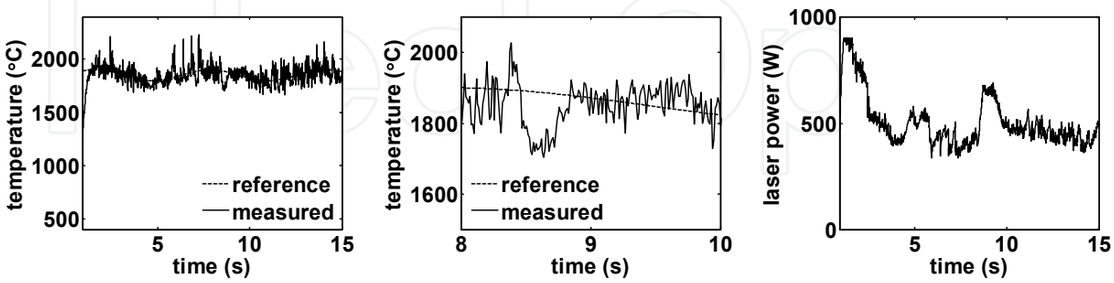

(a) (b) (c)

Fig. 22. Temperature controller results using unfiltered measurement and reference temperature given in equation (44), (a) temperature, (b) zoomed–in view of temperature, and (c) laser power

In the fourth experiment the temperature controller uses the filtered measurement to track the temperature reference given in equation (44). The mass flow rate and traverse speed are 6 g/min and 6 ipm, respectively. The results are shown in Fig. 23. The average absolute error is 40.8 °C and error standard deviation is 55.7 °C. Compared with the results in Fig. 22, the average absolute error is reduced by 22.9% and error standard deviation is reduced by 21.6%. Also, the oscillations in the temperature and laser power signals have been greatly reduced.

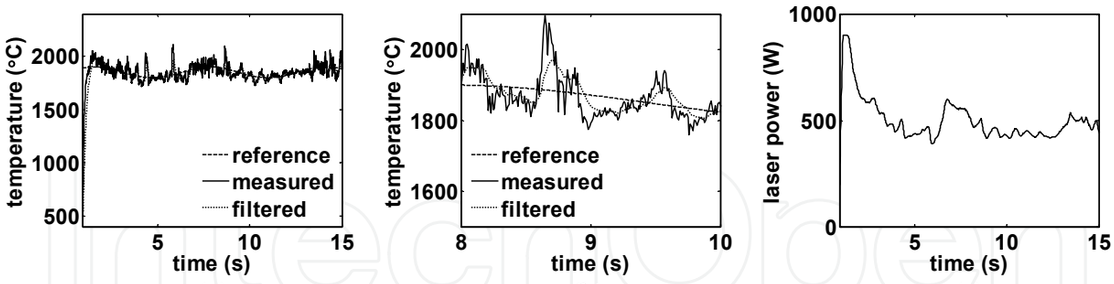

(a) (b) (c)

Fig. 23. Temperature controller results using filtered measurement and reference temperature given in equation (44), (a) temperature, (b) zoomed–in view of temperature, and (c) laser power

5. Summary and conclusions

This chapter presented a methodology, based on stochastic process modeling and Kalman filtering, to filter manufacturing process measurements, which are known to be inherently noisy. Via simulation studies, the methodology was compared to low pass and Butterworth filters. The methodology was applied in a Friction Stir Welding (FSW) process to filter data

used to construct a dynamic axial force process model and by an on–line axial force controller. Also, the methodology was applied to a Laser Metal Deposition (LMD) process to filter data used to construct a dynamic melt pool temperature process model and by an on–line melt pool temperature controller.

The simulation studies demonstrated that the filter methodology was able to reduce signal variation and maintain signal phase and magnitude fidelity better than the low–pass and Butterworth filters. Also, the dynamic response generated from the model constructed from data processed with the filtering methodology was closer to the true response than those generated from models constructed from data processed with the low–pass and Butterworth filters. The experimental results demonstrated that models for the FSW and LMD process constructed from data processed by the filtering methodology provided more accurate responses than models constructed from the raw data. Also, when the filtering methodology was used to process the measurements in the FSW and LMD controllers, better closed–loop response was realized as compared to the closed–loop response when implementing the controllers using unprocessed measurements.

6. References

Åström, K.J. and Wittenmark, B., 1995, Adaptive Control, Addison–Wesley, New York.

Bhattacharyya, P. and Sengupta, D., 2007, "Estimation of Tool Wear Based on Adaptive Sensor Fusion of Force and Power in Face Milling," *International Journal of Production Research*, Vol. 43, pp. 1–17.

Freitag, K.P., 2004, "Two–Axis Force Feedback Deflection Compensation of Miniature Ball End Mills," Mechanical Engineering Department, North Carolina State University.

Ghosh, N., Ravi, Y.B., Patra, A., Mukhopadhyay, S., Paul, S., Mohanty, A.R., and Chattopadhyay, A.B., 2007, "Estimation of Tool Wear during CNC Milling Using Neural Network Based Sensor Fusion," *Mechanical Systems and Signal Processing*, Vol. 21, pp. 466–479.

Liang, M., Yeap, T., Rahmati, S., and Han, Z., 2002, "Fuzzy Control of Spindle Power in End Milling Processes," *International Journal of Machine Tools and Manufacture*, Vol. 42, pp. 1487–1496.

Liou, F.W., Slattery, K., Kinsella, M., Newkirk, J., Chou, J–N., and Landers, R.G., 2007, "Applications of a Hybrid Manufacturing Process for Fabrication of Metallic Structures," *Journal of Rapid Prototyping*, Vol. 13, No. 4, pp. 236–244.

Mishra, R.S. and Ma, Z.Y., 2005, "Friction Stir Welding and Processing," *Materials Science and Engineering: R*, Vol. 50, No. 1–2, pp. 1–78.

Kalman Filter Recent Advances and Applications

Edited by Victor M. Moreno and Alberto Pigazo

ISBN 978-953-307-000-1
Hard cover, 584 pages
Publisher InTech
Published online 01, April, 2009
Published in print edition April, 2009

The aim of this book is to provide an overview of recent developments in Kalman filter theory and their applications in engineering and scientific fields. The book is divided into 24 chapters and organized in five blocks corresponding to recent advances in Kalman filtering theory, applications in medical and biological sciences, tracking and positioning systems, electrical engineering and, finally, industrial processes and communication networks.

How to reference

In order to correctly reference this scholarly work, feel free to copy and paste the following:

Thomas Oakes, Lie Tang, Robert G. Landers and S. N. Balakrishnan (2009). Kalman Filtering for Manufacturing Processes, Kalman Filter Recent Advances and Applications, Victor M. Moreno and Alberto Pigazo (Ed.), ISBN: 978-953-307-000-1, InTech, Available from: http://www.intechopen.com/books/kalman_filter_recent_adavnces_and_applications/kalman_filtering_for_manufacturing_processes

INTECH
open science | open minds

InTech Europe
University Campus STeP Ri
Slavka Krautzeka 83/A
51000 Rijeka, Croatia
Phone: +385 (51) 770 447
Fax: +385 (51) 686 166
www.intechopen.com

InTech China
Unit 405, Office Block, Hotel Equatorial Shanghai
No.65, Yan An Road (West), Shanghai, 200040, China
中国上海市延安西路65号上海国际贵都大饭店办公楼405单元
Phone: +86-21-62489820
Fax: +86-21-62489821

IntechOpen